Supplementary Information

1 Simulation Methods

1.1 Molecular Dynamics simulations of bulk nanocrystalline Ni samples

We performed molecular dynamics (MD) simulations with an embedded atom method (EAM) [1] potential for Ni [2], which has been demonstrated to provide a reasonable description of the structural and elastic properties of Ni [3]. All simulations were performed by using the MD code LAMMPS developed by Sandia National Laboratories [4]. The time step in all simulations was chosen to be 1 fs. Using a cube-axis oriented 3-D periodic cell with a side length of 1.76 nm of fcc Ni, the elastic constants of bulk Ni at 300 K were first calculated as a reference. MD calculations with a constant number of atoms, constant volume, and constant pressure (NPT) at 0 GPa and 300 K for 50 ps were first used to equilibrate the sample at room temperature. To calculate the anisotropic elastic constants, c_{11} and c_{12}, a simple uniaxial tensile strain rate of $\dot{\varepsilon} = 2.84 \times 10^{7} s^{-1}$ was applied along the x direction with an NVT ensemble at 300 K. The strains in the y- and x- directions were both controlled to be zero under the NVT ensemble. Using the resultant average stresses, σ_{ij}, the elastic constants were obtained from:

$$c_{11} = \sigma_{xx} / \varepsilon \ , \tag{S1}$$

$$c_{12} = (\sigma_{yy} + \sigma_{zz}) / 2\varepsilon . \tag{S2}$$

where the strain ε is given by $\dot{\varepsilon} t$, where t is the simulation time.

The system was then compressed in the [110] direction at the strain rate of $\dot{\varepsilon} = 2.84 \times 10^{7} s^{-1}$. As the strain ε applied in [110] is equivalent to $\varepsilon_{xx} = \varepsilon_{yy} = \varepsilon/2$, $\varepsilon_{xy} = \varepsilon$, C_{44} can be extracted as::

$$c_{44} = \sigma_{xy} / \varepsilon . \tag{S3}$$

The bulk modulus B is calculated to be: $B = \frac{1}{3}(c_{11} + 2c_{12})$[5].

To simulate bulk nanocrystalline Ni, five samples with periodic boundary conditions (PBC) in all 3 directions, with grain sizes of 2.2, 3.4, 4.6, 7 and 10.5 nm were constructed. The side length of these cubic samples ranged from 3.52 nm to 10.56 nm, such that each computational cell contained 64 grains. Energy minimization via the conjugate gradient method was applied to attain an equilibrium configuration at 0 K [6]. The structure was then annealed at a temperature of 300 K, and the pressure was controlled to be 0 GPa with NPT ensemble for 50 ps. A constant pressure between 0 GPa to 20 GPa was applied to the system for 200 ps at 300 K to calculate the isothermal bulk modulus using:

$$B = -V \left(\frac{\partial P}{\partial V}\right) . \tag{S4}$$

Analogous steps were carried out through equilibration to calculate the Young's modulus of bulk nanocrystalline Ni. After relaxing the structure with an NPT ensemble at 0 GPa and 300 K for 50 ps, a uniform uniaxial tensile loading was applied in the x-direction by extending the simulation box length at the strain rate of $\dot{\varepsilon} = 1.0 \times 10^{6} s^{-1}$. During this straining, the NPT ensemble was maintained at 300K, and the pressure in the y and z directions was kept at 0 GPa to allow the Poisson contraction. The range of pressures was chosen to be from 0 to 1 GPa with five data points to ensure the sample remained in the harmonic regime [7, 8]. The Young's modulus was calculated from the loading slope of the tensile stress-strain data.

1.2. Finite Elements Simulations of nanocrystalline Ni thin film samples

Finite Elements (FE) meshes for polycrystalline film samples were generated by assembling N_x x N_y x N_z cubic grains, each with 2 nm dimensions. N_x=N_y=3 and N_z=1, 2, 5, 10, 20 were used for the simulations. Each grain had cubic symmetry and was initially assigned a random crystallographic orientation [9]. The elastic constants were provided by the MD simulations (see section 3.1). Perfect inter-granular bonding was assumed and no explicit modeling of the grain boundaries was performed. The commercial package Abaqus with the linear hexahedral elements with reduced integration (C3D8R) was used for all FE simulations, As in MD simulations, the film thickness was positioned along the z-direction. To simulate uniaxial stretching of an infinite film, unconstrained on both sides, the following boundary conditions were imposed as shown in Figure S 1:

- On face +x: $u_x = 0.006$ nm
- On face -x: $u_x = 0$
- On face +y: $u_y = uniform$
- On face -y: $u_y = 0$
- On face +z: free
- On face -z: free

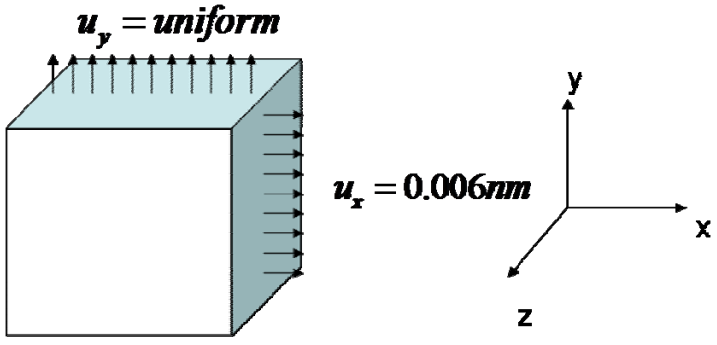

Figure S 1. An illustration of polycrystalline film sample for the FE simulations, with boundary conditions applied in x, y and z directions.

These boundary conditions guaranteed that $\sigma_y = \sigma_z = 0$ (this condition is satisfied for each element if all grains are isotropic, and as an integral on the sample sides for the case of anisotropic grains). The reaction force necessary to impose the prescribed displacement on the +x face, F_x, was extracted from the analysis, and the Young's modulus was calculated as:

$$E_x = \frac{F_x}{A_x}\frac{L_x}{u_x} \qquad \text{(S5)}$$

where A_x is the area of the +x face of the crystal and L_x the length of the crystal along the x-direction ($L_x = d \cdot N_x$). A grain size, $d = 2nm$ was used in all simulations for the convenience of dimensional comparison with MD simulation results, although the elastic properties extracted by the FE simulations are obviously size-independent.

To verify that these conditions yielded the correct modulus, a simple check was performed for an isotropic material. A 3x3x1 crystal was built following the outlined procedure, but the shear modulus c_{44} was chosen as $c_{44} = (c_{11} - c_{12})/2$ to enforce isotropy. For such a material, the isotropic modulus predicted by Eqn (S7) (see sec. 2.1) was 136.094 GPa. The FE calculated value was 136.093 GPa, which is essentially identical to the theoretical value.

1.3 Molecular Dynamics simulations of bulk and thin film nanocrystalline Diamond samples

Unlike Ni, diamond has directional covalent bonding with a much higher cohesive energy of -7.37 eV/atom. The modified embedded atomic method (MEAM) potential [10] was used, and all simulations were conducted using LAMMPS code. MEAM potential parameters are given in Table S 1.

Table S 1. The MEAM potential parameters of diamond. The names of parameters are described in Ref. [11].

Elt	'C'	esub	7.37
lat	'dia'	asub	1.0
z	4.0	$t^{(0)}$	1.0
ielement	6	$t^{(1)}$	5.1
atwt	12.0111	$t^{(2)}$	9.8
α	4.14	$t^{(3)}$	-0.57
$b^{(0)}$	4.1	rozero	1.0
$b^{(1)}$	3.0	ibar	0
$b^{(2)}$	1.5	rc	3.0
$b^{(3)}$	1.0	augt1	0
alat	3.567	attract(1,1)	-1.0

2 Results

2.1. Calculation of elastic constants of single crystalline Ni and diamond

The elastic constants calculated by MD at 300 K are given in Table S 2. Agreement with experiment [3, 12] was expected because the EAM functions were determined by fitting to the elastic constants at 0 K.

Table S 2. Comparison of elastic constants from (M)EAM calculation and Experimental data

		C_{11} (GPa)	C_{12} (GPa)	C_{44} (GPa)	B (GPa)
Diamond	MEAM	1075.7	116.35	590.1	436.1
	Expt [12].	1084.4	127.0	576.6	446.1
Nickel	EAM	248	148	126	181
	Expt[3].	247	147	125	180

The Young's modulus along the <100> crystal direction is defined as: $E_{<100>} = \sigma_{11} / \varepsilon_{11}$ where $\sigma_{ij} = \sigma_{11}\delta_{i1}\delta_{j1}$. This leads to: $E_{<100>} = 1/s_{11} = \frac{c_{11}^2 + c_{11}c_{12} - 2c_{12}^2}{c_{11} + c_{12}} = 136$ GPa, where the compliance tensor is $\mathbf{s} = \mathbf{c}^{-1}$. The Young's modulus in any other direction can be calculated as [13]:

$$E_{<hkl>} = \frac{1}{s_{11} - 2\left(s_{11} - s_{12} - \frac{1}{2}s_{44}\right)\left(h^2k^2 + h^2l^2 + k^2l^2\right)} \qquad \text{(S6)}$$

where the unit vector defining the direction <hkl> is (h,k,l). It is easily demonstrated that the stiffest direction is <111>, for which the obtained anisotropic elastic modulus, $E_{<111>} = 305$ GPa.

For a polycrystalline Ni sample with no specific texture, it is reasonable to assume that the modulus can be well represented by the average of Eqn (S6) over the full solid angle. Using an isostrain (Reuss) model [14], and noting that:

$$< h^2k^2 + h^2l^2 + k^2l^2 >= \frac{1}{4\pi}\int_{-\pi/2}^{\pi/2}\int_{-\pi}^{\pi}(h^2k^2 + h^2l^2 + k^2l^2)\cos(\theta)\,d\varphi\,d\theta = \frac{1}{5} \qquad \text{(S7)}$$

where $h=\cos(\theta)\cos(\varphi), k=\cos(\theta)\sin(\varphi), l=\sin(\theta)$, we obtain a lower bound for the modulus of an isotropic Ni polycrystal:

$$E_{lb}=\frac{5}{3s_{11}+2s_{12}+s_{44}}=205\ \text{GPa} \tag{S8}$$

Similarly, an isostress (Voigt) model [14] yields an upper bound:

$$E_{ub}=\frac{c_{11}-c_{12}+3c_{44}}{2c_{11}+3c_{12}+c_{44}}\left(c_{11}+2c_{12}\right)=242\ \text{GPa} \tag{S9}$$

The lower bound estimate is in good agreement with typical experimental data ($E_{\text{exp}}\simeq 200$ GPa [15]).

2.2. Bulk and Young's moduli of bulk nanocrystalline Ni

The isothermal bulk modulus for nanocrystalline Ni with the grain sizes of 2.2, 4.6 and 7 nm was calculated by using Eqn (S4). The range of pressures was chosen to be from 0 to 1 GPa to ensure the harmonic regime [7, 8]. The bulk modulus was calculated to be 165.7 GPa for the 2.2 nm-grained sample, 167.9 GPa for the 4.6 nm-grained sample, and 179.3 GPa for the 7 nm-grained bulk nanocrystalline Ni sample. Figure S 2 shows the ratio of the calculated bulk modulus (normalized by a typical experimental value for microcrystalline bulk Ni (181 GPa [16])) as a function of decreasing grain size. The plot in Figure S 2 clearly shows that both the bulk and the Young's moduli are weakly dependent on the grain size in the range studied, with the smaller grain sizes generally resulting in lower moduli. For example, the 2.2 nm-grained sample has a bulk modulus 8.45% lower than the experimentally-determined one; while in the 7 nm-grained sample this difference is virtually indistinguishable. This suggests that smaller-grained samples may exhibit higher compressibility likely due to the higher volume fraction of grain boundaries, where the

interatomic bonds are more compliant as compared with the grain interior. The Young's modulus was also found to decrease from 174.5 GPa down to 117.1 GPa with the grain size reduction from 10.5 nm to 2.2 nm. The relative amount of Young's modulus decrease, 41.5%, was much more substantial than the 8.45% reduction in the bulk modulus over the same range of grain sizes. This might be explained by the more compliant response of grain boundary bonds under shear loading. The stress state in the bulk modulus simulations was completely hydrostatic, and therefore contained no shear components. In contrast, the loading condition for the Young's modulus calculations introduced shear stress and strain components, leading to a more pronounced size effect.

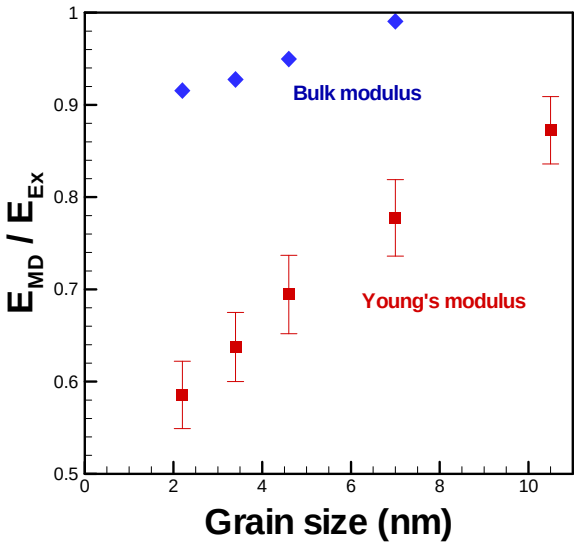

Figure S 2. Bulk and Young's moduli calculated by MD simulations and normalized by their respective experimental values vs. grain size. Experimental data were extracted from Refs [15, 16].

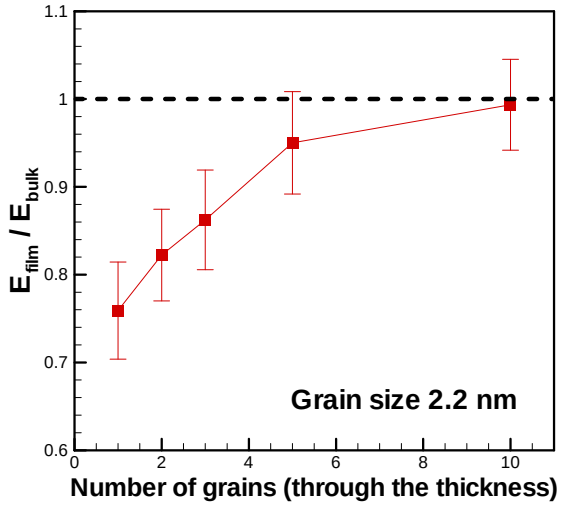

Figure S 3. Young's modulus dependence on the film thickness of 2.2 nm grained nanocrystalline Ni thin film. Each data point was averaged from 5 samples with error bars.

2.3. MD simulations of Young's modulus of nanocrystalline Ni thin films

Figure S 4 displays the in-plane Young's modulus normalized by the calculated Young's modulus for the bulk 2.2nm nanocrystalline Ni, as a function of film thickness, expressed in terms of the number of grains, for all the films simulated. The Young's moduli of nanocrystalline Ni films with thicknesses of 35.2 nm and below were found to be lower than those of the bulk nanocrystalline Ni. Films with the thicknesses of ~10 grains had close-to-macroscale Young's modulus while the 1 grain-thick samples exhibited a ~24.1% reduction in the Young's modulus as compared with bulk.

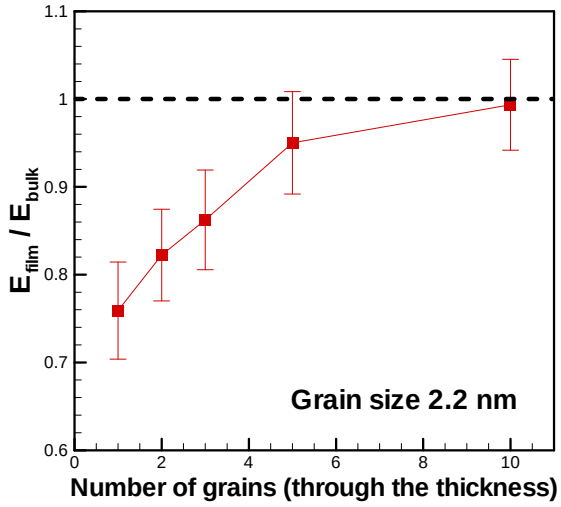

Figure S 4. Young's modulus dependence on the film thickness of 2.2 nm grained nanocrystalline Ni thin film. Each data point was averaged from 5 samples with error bars.

2.3. Continuum effects (Finite Elements simulation results)

To ascertain whether any continuum effects could be partly responsible for the observed size effect in the Young's modulus of thin nanocrystalline Ni films, Finite Elements simulations of thin films with 1-20 grains across the thickness were performed as described in sec1.2 The Young's modulus of the thin film samples as a function of the number of grains through the thickness is presented in Figure S 5. Lower (Eqn (S8)) and upper (Eqn (S9)) analytical limits for isotropic averages bound the results, as expected. Each sample has $3x3xN_z$ grains, with the number of grains through the thickness, $N_z = 1, 2, 5, 10, 20$. Each data point is the average of 5 nominally identical simulations, only differing by the randomly assigned grain orientations. Error bars are displayed for each data point. Figure S 6 illustrates some representative meshes with Mises stress distributions.

Clearly evident from Figure S 5 is the absence of any noticeable size effect. This implies that the strong dependence of the Young's modulus on the film thickness brought to light by the MD simulations (Figure S 4) is not a continuum effect and is likely attributed entirely to the surface effects described above. Somewhat surprisingly, all FE simulations showed the elastic moduli 6-9% larger than the isotropic average predictions. This is likely a result of the constraining conditions on the y and z faces, which are forced to remain planar and parallel (although allowed to expand/contract to guarantee an average uniaixial stress condition), hence heavily constraining the boundary grains in the system.

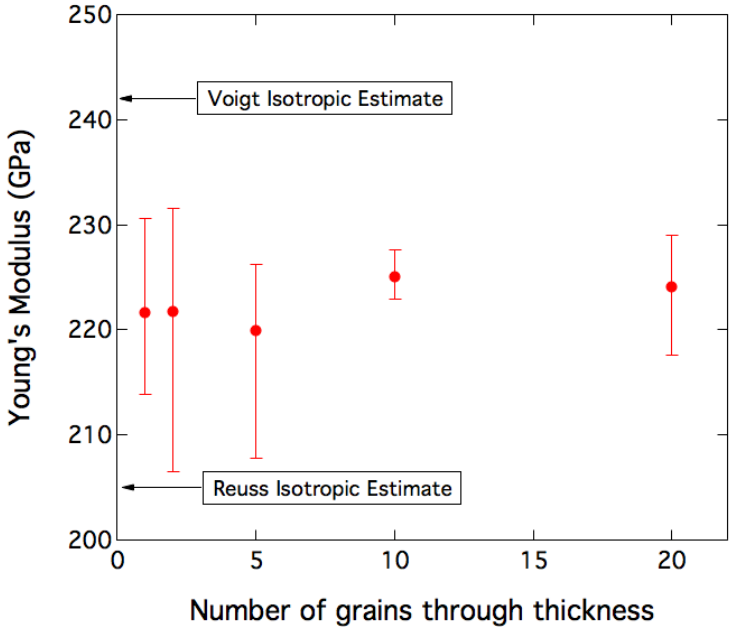

Figure S 5. Finite Elements prediction of the elastic modulus of the film as a function of the number of grains through the thickness. Upper (Voigt) and lower (Reuss) limits for isotropic averages bound the results, as expected. The grain size used in the simulation is 2nm, although the problem is size independent. Notice the lack of discernible size effect, confirming that the strong dependence of the modulus on film thickness from MD calculations (Figure S 4) is not a continuum effect.

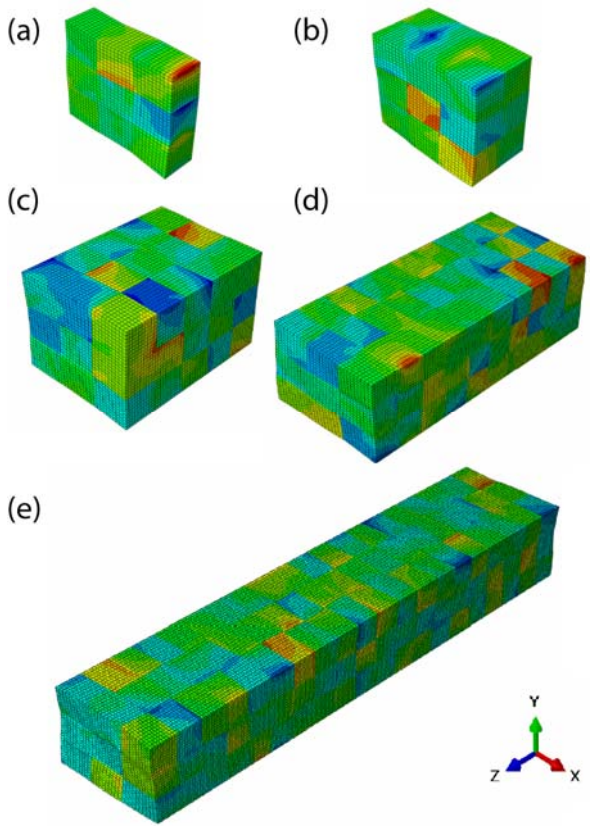

Figure S 6. Representative meshes of polycrystalline thin films loaded in uniaxial tension. The contours represent the stress distribution along the loading direction (σ_{xx}) in the grains. The film thickness is in the z direction. (a) 3x3x1; (b) 3x3x2; (c) 3x3x5; (d) 3x3x10; (e) 3x3x20.

2.4 MD simulations of Young's modulus of nanocrystalline Diamond

The MD simulations of tensile elastic response of nanocrystalline Ni revealed a strong dependence of the Young's modulus on both the grain size and the film thickness. The spatial profile of the local Young's moduli, shown in Figure 3, demonstrated that the atomic structures within the grain boundaries and in the vicinity of the free surface were more compliant than those in the grain interior. These findings suggest that the regions within a material, where the local spacing among the atoms is larger than the equilibrium distance, deform elastically more readily than the equilibrium-positioned portions (atoms at the free surface can be regarded to be infinitely apart

from their neighbors along the outward normal direction of the surface). This relationship between the atomic structure and the ensuing mechanical response has been linked to the shape of the interatomic potential curve because the elastic properties are closely related to the second derivative of the potential curve with respect to the interatomic distance [17]. Comparing the influence of grain size and thin film thickness on the elastic properties between nanocrystalline Ni and a material, whose bonding energetics are vastly different from those of Ni, could help shed light on the underlying physics behind these phenomena.

Figure S 7 shows the Young's modulus of diamond as a function of both the grain size and the film thickness, calculated by both methods (see section 2.3). Note that comparing the stress level of dashed lines can show the grain size effects on Young's modulus of bulk diamond. This plot reveals that the effects of both the grain size and the film thickness also exist in nanocrystalline diamond: Young's modulus decreases with the reduction in either parameter. The results of stress-strain method (10^{-1} strain), (M1) are shown to agree with those of long time NPT method (~10^{-3} strain) (M2), ensuring that the deformation in both methods is done in an elastic regime.

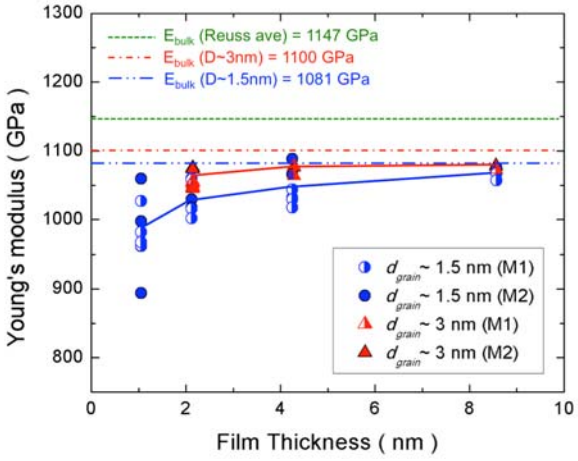

Figure S 7. Young's modulus of nanocrystalline diamond as a function of grain size and film thickness. Dashed lines represent Young's modulus of bulk forms, with the green one corresponding to the coarse-grained polycrystalline diamond calculated by Reuss average in equation (S8). In the legend, M1 stands for the stress-strain method and M2 stands for the long time NPT method.

2.3 Discussions

Young's modulus is proportional to the second derivative of the potential energy curve with respect to the interplanar spacing of crystallographic planes, whose normal is parallel to the axial loading direction. If the potential energy curve is harmonic, the Young's modulus remains constant regardless of the interplanar spacing. In real materials, the shape of the potential energy curves is usually anharmonic. The Young's modulus of grain boundaries, which usually accommodate a certain amount of free volume, and hence have higher-than-equilibrium atomic spacing, is expected to be lower than that of the grain interior. The discrepancy between the Young's moduli in the grain boundary vs. grain interior is correlated with the amount of anharmonicity in the potential energy curve and may explain the different Young's moduli reduction between Ni and diamond studied here. The finite element analysis performed in section 3.5 does not have the information of the potential energy curve with respect to the location in the samples. Thus, it is not surprising that the results of the finite element analysis did not show any length scale effect.

To quantify the degree of harmonicity, we studied the potential energy variation during the separation of two rigid crystalline blocks. This approach is preferred to the more typical analysis of two neighboring atoms, as it better captures the Young's modulus of volumetric samples. We cleaved the surfaces along the (001), (111) and (110) crystallographic planes, and then computed the potential energy as a function of the separation distance, δ (see Figure S 8(a)). These three

particular planes represent some of the most common orientations, and serve as reliable model surfaces for the potential energy quantification. The simulation block sizes were $12[100]\times4[010]\times10.5[001]$, $12[11\bar{2}]\times4[\bar{1}10]\times10.5[111]$ and $12[111]\times4[11\bar{2}]\times10.5[\bar{1}10]$. Figure S 8(a) shows an example of such a potential energy curve as a function of separation distance for the separation on the (001) plane for Ni, and Figure S 8(b) shows its second derivative, $(\partial^2 E_{pot}/\partial\delta^2)$. Both variables in the plot are normalized by their respective equilibrium values, denoted by the subscript "0," to avoid the effects of simulation cell size. A greater degree of anharmonicity in the potential curve would result in a more pronounced drop in curvature at larger δ/δ_0.

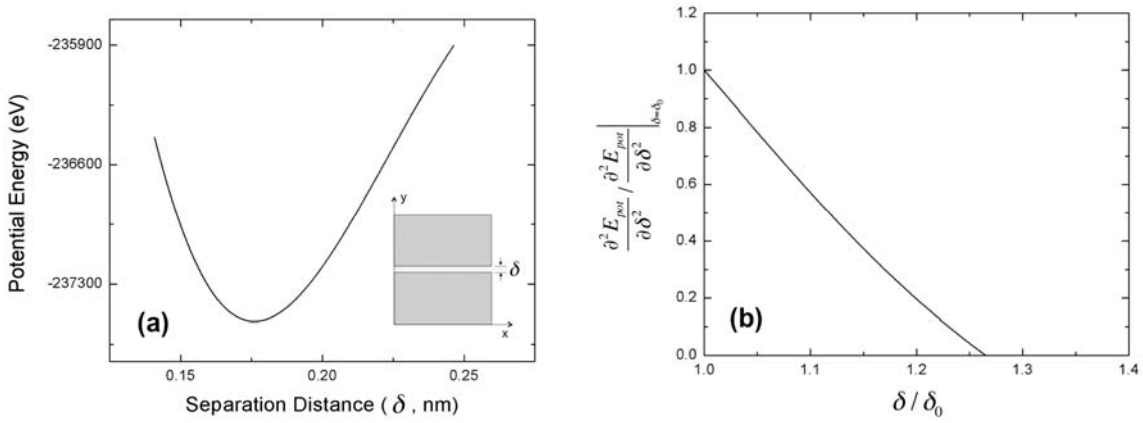

Figure S 8. (a) The potential energy variation of Ni with respect to the separation distance between two crystalline blocks (δ) for (001) plane. (b) Curvature of the potential energy shown in (a) as $\frac{\partial^2 E_{pot}}{\partial\delta^2}\Big/\frac{\partial^2 E_{pot}}{\partial\delta^2}\Big|_{\delta=\delta_0}$ a function of the separation distance. Both x- and y-axes are normalized by their equilibrium values for comparison between two different materials (Ni and diamond)

Following this methodology, the second derivatives of the potential energy curves for the separation along (001), (111), and (110) planes for Ni and diamond are shown in Figure S 9. These plots consistently demonstrate that the curvature of the potential curve for Ni falls off with separation distance more rapidly than that for C. This result implies that the potential curve of Ni is more

anharmonic than that of diamond, and that for a given atomic spacing (δ/δ_0), the effects of grain size on Young's modulus are stronger for nanocrystalline Ni than for nanocrystalline diamond. These findings are consistent with the simulations performed in this work (Figure 2 (a) and Figure S 7).

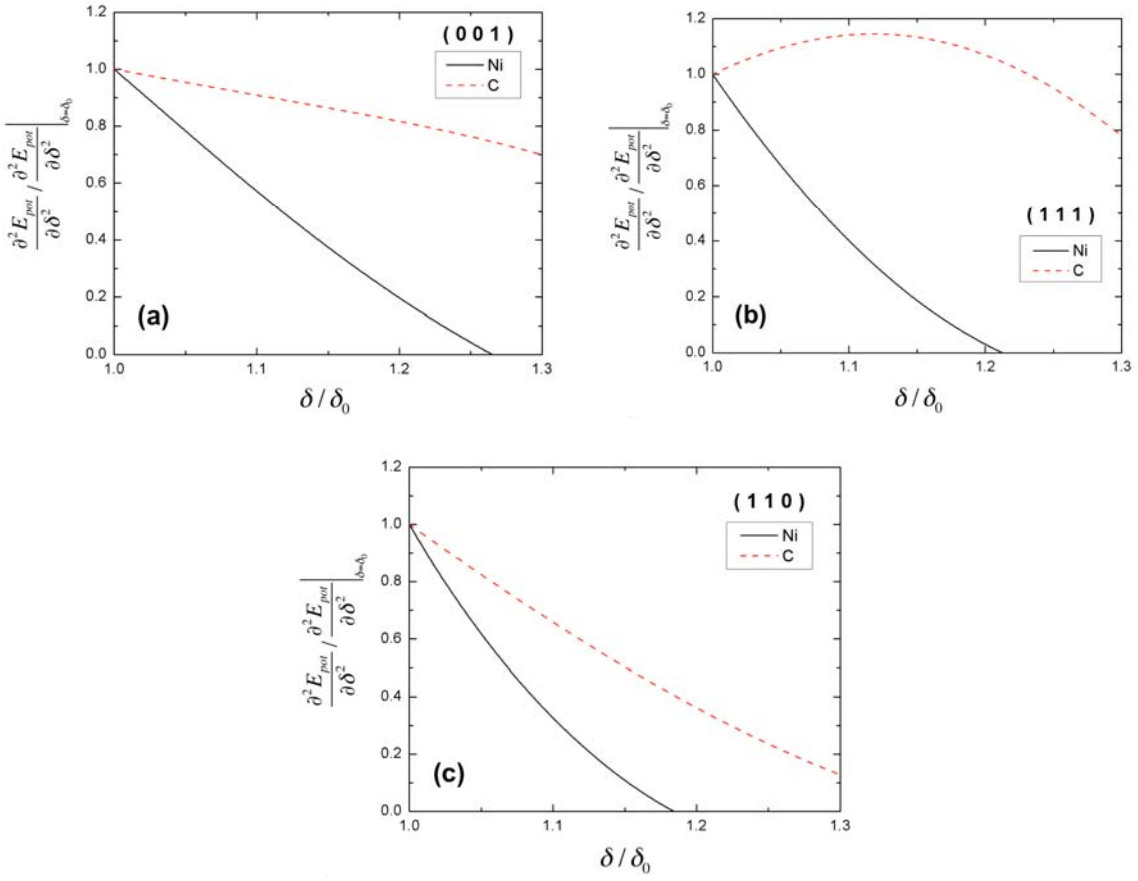

Figure S 9. Curvature of the potential energy curves as a function of normalized separation distance along (a) (001), (b) (111) and (c) (110) planes.

Our simulations demonstrate that the Young's modulus decreased with decreasing film thickness, which suggests its dependence on the film-thickness-to-grain size ratio (t/d). Similar "smaller is weaker" trend in the yield strength has only been observed in a size-dependent study in nanocrystalline Ni nanopillars [18], whereby nanocrystalline Ni–4%W nanopillars with grain sizes of 60nm exhibited a "smaller is weaker" trend at smaller D/d's. Recent work on the deformation of

nanocrystalline Pt nanopillars conveyed a different phenomenon, that the yield strength remained similar to its bulk value for the range of D/d's from ~96 down to 8 [19], which suggests that the absolute grain size, in addition to the t/d ratio, could also plays an important role in the size effects. While recent studies on the nanocrystalline pillars revealed that both D/d and the grain size could both affect the yield strength of materials, more computational and experimental studies could be performed to investigate the elastic modulus' dependency on both grain size and t/d ratio in the future.

References

[1] M.S. Daw, M.I. Baskes, Phys Rev B 29 (1984) 6443.
[2] Y. Mishin, D. Farkas, M.J. Mehl, D.A. Papaconstantopoulos, Phys Rev B 59 (1999) 3393.
[3] G. Simons, H. Wang, Single Crystal Elastic Constants and Calculated Aggregate Properties, in, MIT Press, Cambridge, MA, 1977.
[4] S. Plimpton, J Comput Phys 117 (1995) 1.
[5] R. Hill, Proc. Phys. Soc. London A65 (1952) 349.
[6] W.H. Press, S.A. Teukolsky, W.T. Vertterling, B.P. Flannery, Numerical Recipes in Fortran: The Art of Scientific Computing, 2nd ed., Cambridge University Press, New York, 1992.
[7] T. Song, X.W. Sun, R.F. Wang, H.W. Lu, J.H. Tian, P. Guo, Physica B: Condensed Matter 406 (2011) 293.
[8] L.M. Thomas, J. Shanker, physica status solidi (b) 189 (1995) 363.
[9] R.M. Brannon, Available at http://www.mech.utah.edu/~brannon/public/rotation.pdf (2002).
[10] M.I. Baskes, Phys Rev B 46 (1992) 2727.
[11] http://lammps.sandia.gov/doc/pair_meam.html (LAMMPS official website).
[12] E.S. Zouboulis, M. Grimsditch, A.K. Ramdas, S. Rodriguez, Phys Rev B 57 (1998) 2889.
[13] M.A. Meyers, K.K. Chawla, in: Mechanical Behavior of Materials (2nd Ed.), Cambridge University Press, 2009.
[14] T.H. Courtney, in, McGraw-Hill, 2nd edition, 2000.
[15] http://en.wikipedia.org/wiki/Nickel (Available at).
[16] S. Rekhi, S.K. Saxena, R. Ahuja, B. Johansson, J. Hu, J Mater Sci 36 (2001) 4719.
[17] C.R. Barrett, W.D. Nix, A.S. Tetelman, The principles of Engineering Materials, Prentice Hall Inc., 1973.
[18] D. Jang, J.R. Greer, Scripta Materialia 64 (2011) 77.
[19] X.W. Gu, Z. Wu, Y. Zhang, D.J. Srolovitz, J.R. Greer, To be submitted.